



## Efficient Co@CoO core-shell nanocrystals as catalysts for visible-light-driven water oxidation

Zheng Wan<sup>a</sup>, Qian Xu<sup>a</sup>, Hui Li<sup>a</sup>, Yi Zhang<sup>c</sup>, Yong Ding<sup>b,\*</sup>, Jide Wang<sup>a,\*</sup>

<sup>a</sup> Key Laboratory of Oil and Gas Fine Chemicals, Ministry of Education & Xinjiang Uygur Autonomous Region, College of Chemistry and Chemical Engineering of Xinjiang University, Urumqi 830046, China

<sup>b</sup> State Key Laboratory of Applied Organic Chemistry, Key Laboratory of Nonferrous Metals Chemistry and Resources Utilization of Gansu Province and College of Chemistry and Chemical Engineering, Lanzhou University, Lanzhou 730000, China

<sup>c</sup> Hunan Provincial Key Laboratory of Efficient and Clean Utilization of Manganese Resources, College of Chemistry and Chemical Engineering, Central South University, Changsha 410083, Hunan, China



### ARTICLE INFO

#### Article history:

Received 19 December 2016

Received in revised form 8 March 2017

Accepted 19 March 2017

Available online 23 March 2017

#### Keywords:

Co@CoO

Core-shell nanocrystals

Photocatalysis

Water oxidation

Visible-light-driven

### ABSTRACT

This paper introduces the first attempt of using well organized Co@CoO core-shell nanocrystals as an alternative toward noble metal catalysts for photocatalytic water splitting reactions. In this work, four kinds of stable magnetic Co@CoO core-shell nanocrystals were fabricated through a one-pot toluene-water two-phase interfacial reaction with oleic acid as a surfactant. The size and shape of the as-prepared crystals can be carefully adjusted through dynamically coating the closely packed monolayer of coordinating ligand onto the growing crystals. It is notable that spherical pine-nut-like hierarchical assemblies of Co@CoO core-shell nanoplates exhibit excellent photocatalytic activity (the maximum value of O<sub>2</sub> yield is over 96%). Even after the sixth run, the high catalytic activity of the recovered Co@CoO core-shell nanoplates remained.

© 2017 Elsevier B.V. All rights reserved.

## 1. Introduction

The photocatalytic water splitting provides an alternative abundant clean and renewable energy sources. Development of photocatalyst is the key technology for converting and storing solar energy [1–4]. Although studies have been widely performed in this field, water oxidation (2H<sub>2</sub>O → 4H<sup>+</sup> + 4e<sup>−</sup> + O<sub>2</sub>) still remains a challenging task during photocatalytic water-splitting process in natural and artificial photosynthesis [5–7].

Efficient water oxidation catalysts containing various metal complexes have been developed [8–15]. Especially cobalt-containing materials have been widely explored because this element is more abundant and less expensive than precious metals, such as ruthenium and iridium [15–19]. For instance, Ding and co-workers demonstrated that Co<sub>3</sub>O<sub>4</sub> porous nanocages derived from metal-organic frameworks presented a superior activity for water oxidation, which was comparable with those of nanostructured Co<sub>3</sub>O<sub>4</sub> clusters supported on mesoporous silica [20]. Lu's group showed that the porous CoOx–carbon hybrid material 700–CoOx–C can act as efficient photochemical and electrochemical

water oxidation catalysts [17]. Our recent work demonstrated that [Co<sub>4</sub>(H<sub>2</sub>O)<sub>4</sub>(HPMIDA)<sub>2</sub>(PMIDA)<sub>2</sub>]<sup>6−</sup> and ZIF-67 can serve as efficient catalysts for water oxidation [18,19]. So far, cobalt-based materials have been considered desirable and promising candidates for the development of efficient water oxidation catalysts. However, Co@CoO core-shell nanocrystals as efficient catalysts for water oxidation have been rarely reported.

Magnetic nanomaterials have been extensively applied due to their unique chemical, physical and electronic properties. Co and its oxides are among the most favorable magnetic nanoparticulate materials because of their unique size-dependent structural, magnetic, electronic, catalytic properties and potential applications. The influence of nanomaterials shape, size and crystal structures on catalytic reactivity has been a topic of successive interest owing to its importance from both fundamental and practical viewpoints. Usually, larger particles always exhibit poor catalytic performance, however, particles have stronger tendency to aggregate when their sizes are very small. Hence, fabrication of hierarchical structures is an effective attempt to maintain the catalytic performance while prevent agglomeration for small size particles. In particular, the spherical pine-nut-like hierarchical assemblies of nanoplates are conducive for catalysis. Therefore, a simple and efficient approach to synthesize hierarchically structured core-shell nanocrystals with efficient catalytic performance and good stability is highly desired.

\* Corresponding authors.

E-mail addresses: [dingyong1@lzu.edu.cn](mailto:dingyong1@lzu.edu.cn) (Y. Ding), [awangjd@sina.cn](mailto:awangjd@sina.cn) (J. Wang).

In this work, we presented a simple method to synthesize the hierarchical structure of Co@CoO core-shell nanocrystals and developed highly efficient heterogeneous catalysts for water oxidation. Stable magnetic Co@CoO core-shell nanocrystals were prepared via a one-pot toluene–water two-phase interfacial reaction, and these products were systematically investigated as water oxidation catalysts for oxygen evolution under visible light irradiation. Our results revealed that the Co@CoO core-shell nanoplates were highly efficient water oxidation catalysts with a high O<sub>2</sub> yield over 96% under optimal conditions. This study confirmed that Co@CoO core-shell nanocrystals with a spherical hierarchical structure are excellent water oxidation catalysts. Our core-shell nanocrystal provided new insights into the Co-based catalysts for visible-light-driven water oxidation. This finding provides an alternative to those who are interested in developing new non-noble catalysts for water oxidation. Insights into this new kind catalyst will inspire researchers to develop other types of magnetic nanomaterials for visible-light-driven water oxidation.

## 2. Experimental section

### 2.1. Chemicals

[Ru(bpy)<sub>3</sub>]Cl<sub>2</sub>, Na<sub>2</sub>S<sub>2</sub>O<sub>8</sub>, oleic acid, and hydrazine hydrate (80%) were obtained from Aladdin. Cobalt (III) acetylacetone (Co(acac)<sub>3</sub>, 99%) was purchased from Adamas. All chemicals were used as received without further purification.

### 2.2. Synthesis of photosensitizers

[Ru(bpy)<sub>3</sub>](ClO<sub>4</sub>)<sub>2</sub> was synthesized by adding an aqueous solution of HClO<sub>4</sub> to an aqueous solution of [Ru(bpy)<sub>3</sub>]Cl<sub>2</sub> [21]. [Ru(bpy)<sub>3</sub>]SO<sub>4</sub> was synthesized by adding one equivalent of Ag<sub>2</sub>SO<sub>4</sub> to an aqueous solution of [Ru(bpy)<sub>3</sub>]Cl<sub>2</sub> [22].

### 2.3. Synthesis of Co@CoO core-shell nanocrystals

In a typical synthesis process, a toluene solution (20 mL) containing 0.035 M Co(acac)<sub>3</sub> and 1 mL of oleic acid was loaded into a 50 mL Teflon-lined stainless steel autoclave. An aqueous solution (20 mL) containing 10 mL of 80% hydrazine hydrate was then transferred to the autoclave to provide a two-phase reaction system. Without stirring the mixture, the autoclave was sealed and maintained at 130 °C for 24 h and then cooled to room temperature naturally. The obtained products were separated by centrifugation at a high speed of 8000 r/min and then washed several times with ethanol and deionized water. Finally, the spherical hierarchical structures of products 1 were dried at 40 °C for 12 h.

The preparation of 2, 3, and 4 is similar to that of 1, except that 0.5 mL, 2.0 mL and 5.0 mL of oleic acid were used instead of 1 mL of oleic acid during the synthesis.

### 2.4. Characterization

Powder X-ray diffraction (PXRD) data were acquired using a Rigaku D/max-ga X-ray diffractometer at a scan rate of 6° min<sup>-1</sup> in 2θ ranging from 15° to 80° with Cu Kα radiation ( $\lambda = 1.54178 \text{ \AA}$ ). Field emission scanning electron microscopy (FESEM) images were obtained using a Hitachi SU8010 microscope operated at 5 kV. High-resolution transmission electron microscopy (HRTEM) images were carried out with a Hitachi-600 TEM at accelerating voltage of 200 kV. Dynamic light scattering (DLS) measurements were measured by Zetasizer Nano S90. UV-vis measurements were performed on a Unico UV-4802S with barium sulfate as reference. X-ray photoelectron spectroscopy (XPS) measurements were

performed on a Thermo Fisher Scientific XPS ESCALAB 250Xi instrument with an Al Kα (1486.8 eV) X-ray source. The concentration of cobalt ion was measured by Atomic Absorption Spectrometry (AAS) on Agilent 240 FS AA.

### 2.5. Visible-light-driven water oxidation

The photocatalytic water oxidation experiment was performed as follows. Different amounts of 1–4 (0 mg to 2 mg) were added in the reaction vessel with a magnetic stirrer, the mixture contained 10 mL of borate buffer solution (80 mM, pH 7.0–10.0), 1.0 mM [Ru(bpy)<sub>3</sub>]<sup>2+</sup>, and 5.0 mM Na<sub>2</sub>S<sub>2</sub>O<sub>8</sub> under illumination at room temperature. The gas in the headspace of the reaction vessel was sampled and then analyzed. To ensure complete air removal, the reaction vessel was sealed with a rubber septum and purged with Ar gas for 5 min. Illumination was performed using a 300 W Xe lamp equipped with a long-pass filter (420 nm cutoff). The evolved O<sub>2</sub> was analyzed by gas chromatography with a thermal conductivity detector (Shimadzu GC-14B) and a 5 Å molecular sieve column (2 m × 4 mm) using Ar as carrier gas.

### 2.6. Electrochemistry

The working electrode was prepared as follows. Co@CoO core-shell nanocrystals 1 (10 mg) and Nafion solution (50 μL) were mixed with 450 μL of ethanol under sonication for 30 min. Afterward, 5 μL of the slurry was transferred onto a glassy carbon electrode, and the electrode was dried in air for 24 h. Electrochemical study was conducted in a typical three-electrode cell by using a platinum wire as counter electrode and Ag/AgCl electrode as the reference electrode. The electrochemical experiments were performed on a CHI600D workstation. The sweep rate was 10 mV s<sup>-1</sup> for cyclic voltammetry (CV) in buffer solutions at room temperature.

## 3. Results and discussion

### 3.1. Characterization of Co@CoO core-shell nanocrystals

Magnetic Co@CoO core-shell nanocrystals samples were synthesized using a one-pot toluene–water two-phase interfacial reaction method. Elemental mapping analysis (Fig. S1, ESI) verifies that the products are composed of Co, O and C elements, indicating the presence of metal Co and cobalt oxide in the sample. The presence of C element is the oleic acid contamination on the surface of nanocrystals, which were prepared in a toluene solution containing Co(acac)<sub>3</sub> and certain volume of oleic acid. Fig. 1 shows the X-ray diffraction (XRD) patterns of the samples. The XRD patterns revealed that the peak positions and relative intensities of all the diffraction peaks for the products were in good agreement with the standard PXRD data. The diffraction peaks in the XRD patterns can be indexed to metallic Co in accordance with JCPDS No. 05-0727. But the existence of CoO could not be observed by the XRD analysis, which can be explained by the small amount of CoO or the amorphous state of CoO.

The detailed element chemical compositions of the prepared samples were further studied by XPS measurements. In the high resolution XPS spectra (Fig. 2), the binding energy of each element was corrected by a C 1s peak (284.8 eV). The peaks at 777.9 and 793.0 eV are ascribed to metallic Co. Two peaks observed at 780.0 and 796.7 eV with two satellite peaks at 786.4 eV and 803.6 eV, respectively, verifying the existence of Co<sup>2+</sup> in the sample. The XPS results clearly demonstrate that the surface of the Co nanocrystals is covered with CoO. The existence of CoO arises from the oxidation of cobalt surface when the sample is exposed to air.

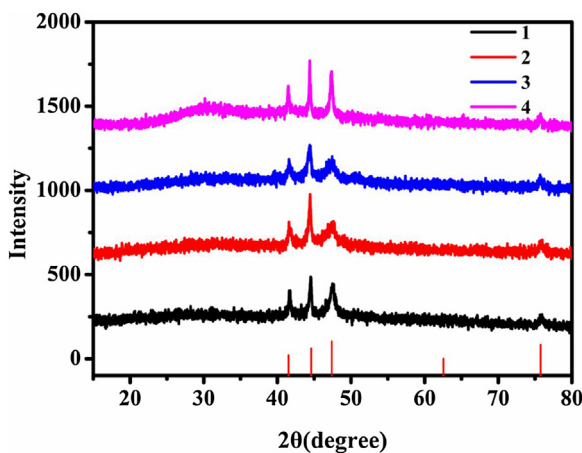


Fig. 1. XRD patterns of Co@CoO core-shell nanocrystals 1–4.

To reveal the detailed structure of the prepared samples, HRTEM image was recorded as shown in Fig. 3 and Fig. S2. The catalyst 1 exhibits two sets of crystalline lattices of 0.19 nm and 0.26 nm, corresponding to the (101) crystal plane of the Co phase and the (111) crystal plane of the CoO phase, respectively, which is consistent with the elemental mapping and XPS analysis results. This characterization confirms that the obtained nanocrystals possess

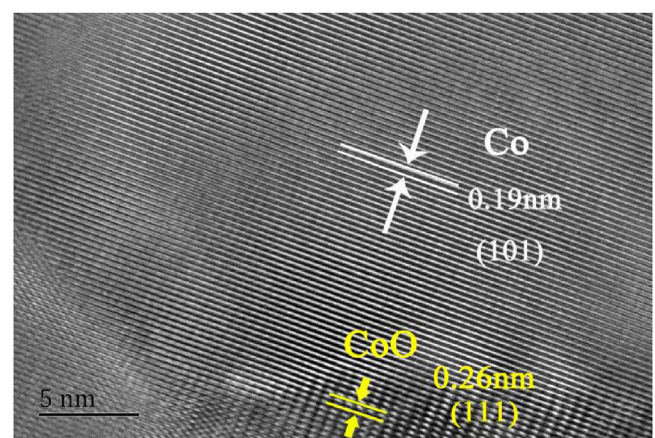


Fig. 3. High-resolution transmission electron microscopy (HRTEM) image of the obtained catalysts 1.

a core@shell structure, Co@CoO. Thus, the prepared samples are referred as Co@CoO nanocrystals.

The morphologies of the obtained products were investigated by FESEM. The FESEM images showed that the products presented four different morphologies (Fig. 4). The morphologies of the obtained nanocrystals were found to be significantly depending on the experimental conditions, particularly the amount of oleic

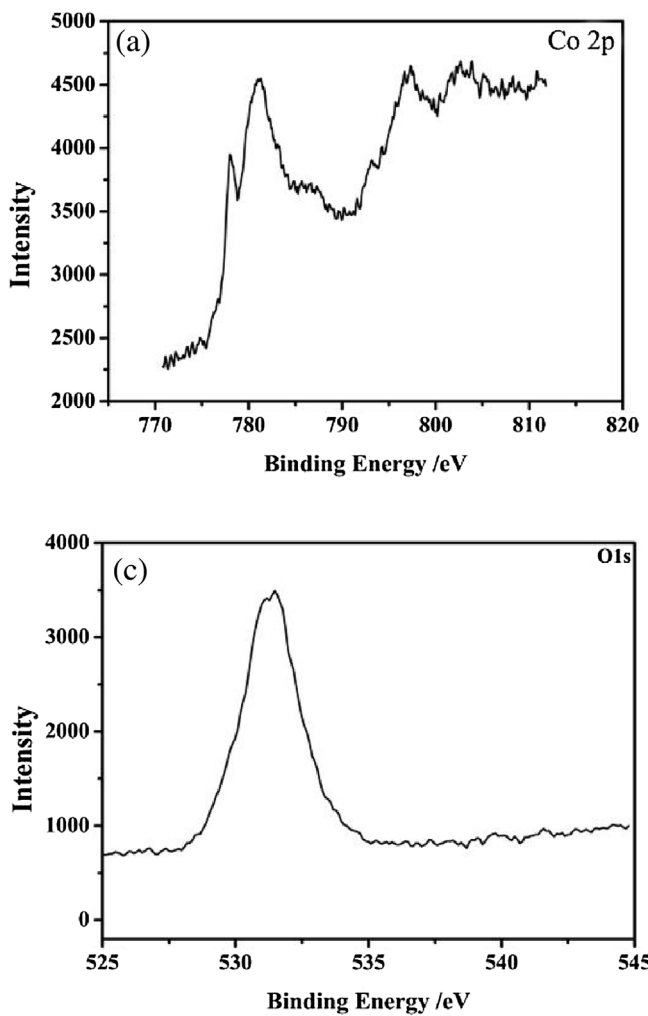
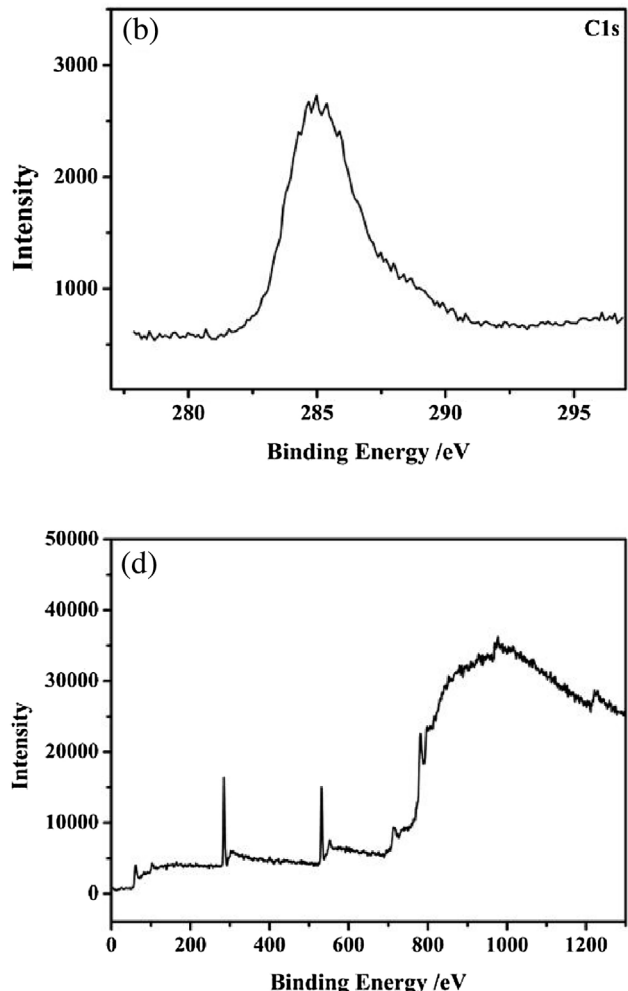
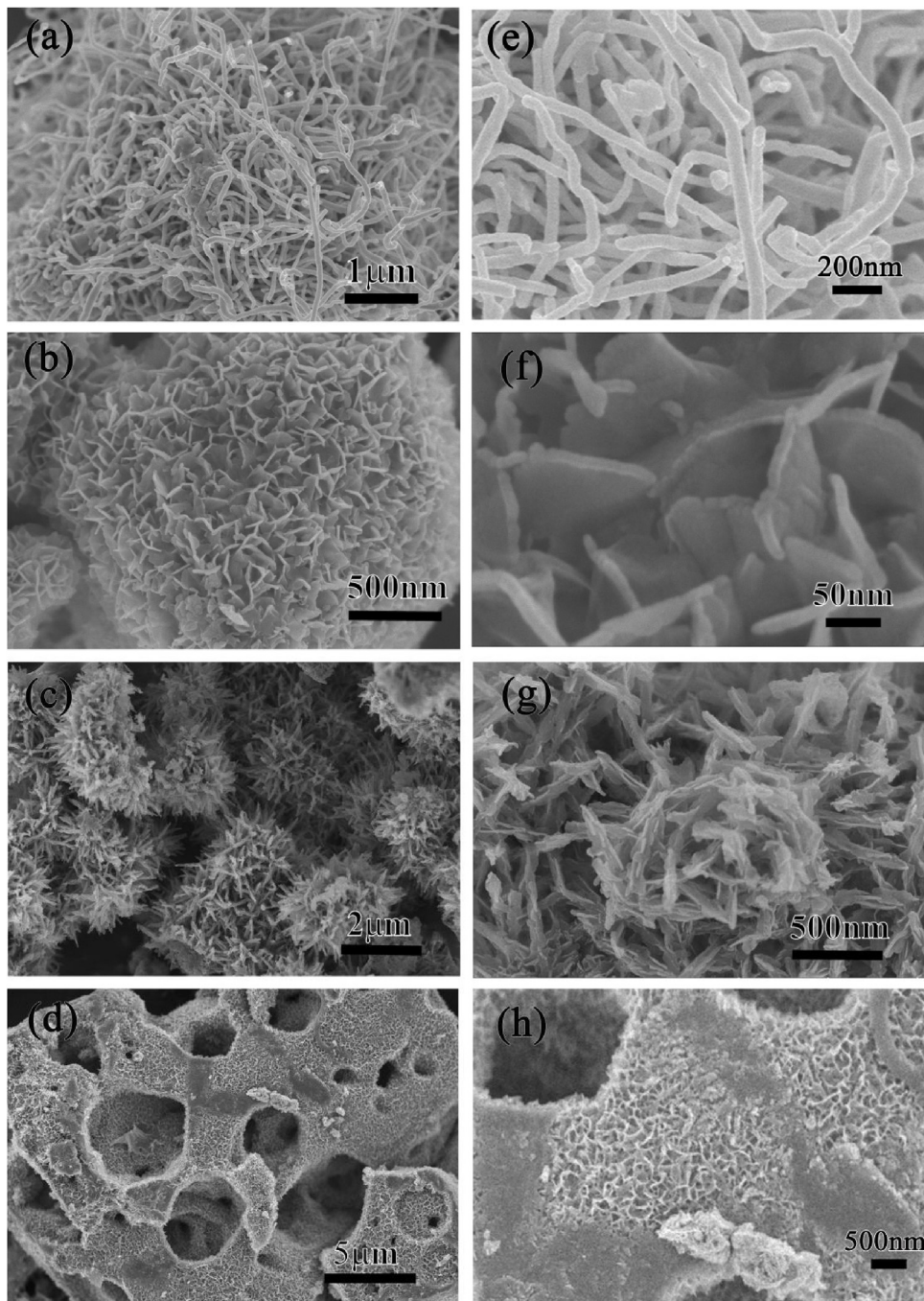


Fig. 2. X-ray photoelectron spectra of catalyst in the energy regions of Co 2p (a), C 1s (b), O 1s (c) and full scan (d) of Co@CoO.





**Fig. 4.** FESEM images of the products 1 (a, e), 2 (b, f), 3 (c, g), 4 (d, h) prepared with 0.5, 1, 2 and 5 mL of oleic acid while keeping the total volume of oleic acid and toluene at 20 mL.

acid. We obtained nanofibers 2 (Fig. 4b, f) when the amount of oleic acid was 0.5 mL. These nanofibers exhibited a mean diameter of approximately 80 nm. When the amount of oleic acid was increased from 0.5 mL to 1 mL, nanoplates 1 with thickness of around 15 nm were produced (Fig. 4a, e). The spherical pine-nut-like hierarchical assemblies of nanoplates were obtained with a diameter of about 2  $\mu$ m. The catalysts 3 prepared with 2 mL of oleic acid showed the presence of urchin-like shape with diameter of approximately 50 nm (Fig. 4c, g). Irregularly porous-shaped products 4 with thickness of around 20 nm (Fig. 4d, h) were also observed in the catalyst prepared with 5 mL of oleic acid. Through the interfacial reaction of  $\text{Co}(\text{acac})_3$  with hydrazine hydrate under hydrothermal conditions, tiny Co crystalline nuclei will be produced and quickly grow

into small-sized nanoparticles. When a crystal grows, various facets will grow with different growth rates, and the growth rates along different directions are proportional to their surface energies [23]. For synthesis in the solution phase, adsorbates such as surfactants, polymers, or halides can interact selectively with various crystal facets and have been applied to alter the surface energy of the specific crystal facet [23–25]. The growth rates of different faces of a Co nanocrystal can be kinetically controlled by tuning the types and concentration of surfactants in the solution, during the adsorption and desorption process, respectively. Oleic acid can selectively adsorb on a certain crystal facet of the as-prepared primary building blocks such as nanoparticles, nanofibers, nanosheets, nanoplates, nanorods, and so on [26]. When bound to nanocrystal surfaces,

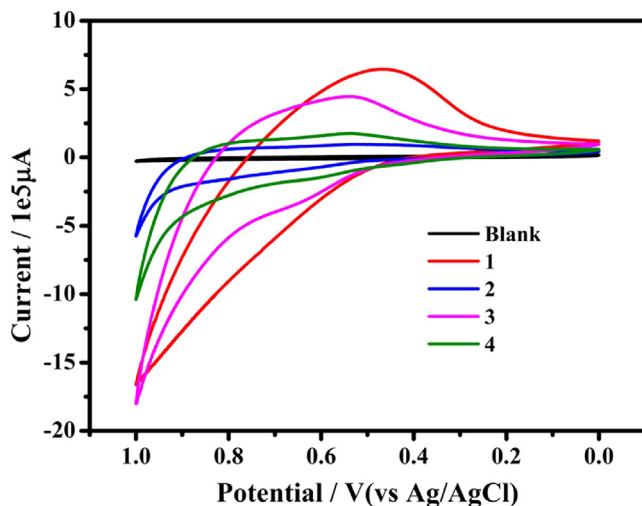


**Fig. 5.** Cyclic voltammogram (CV) of 80 mM sodium borate buffer solution at pH 9.0 with 0.02 g mL<sup>-1</sup> of 1 (red line), 2 (blue line), 3 (pink line) and 4 (green line). The black line displays the CV of 80 mM sodium borate buffer solution at pH 9.0. Conditions: CV was recorded on a CHI600D electrochemical analyser with a glassy carbon pasting and 0.01 mg catalyst, Ag/AgCl, and Pt wire electrodes as the working, reference, and auxiliary electrodes, respectively, at room temperature with a scanning rate of 10 mV s<sup>-1</sup>. (For interpretation of the references to color in this figure legend, the reader is referred to the web version of this article.)

oleic acid molecules provide steric hindrance to molecular addition to the nanocrystals. Therefore, oleic acids effectively prevent these primary building blocks from random aggregation through an entropy-driven self-assemble process. Furthermore, the size and shape of the growing crystals can be gradually adjusted by adding different amounts of oleic acid. The SEM results demonstrate that low concentrations of oleic acid are favorable for the generation of regular morphology for the product. This phenomenon is mainly affected by the nucleation, growth, and diffusion of cobalt crystallites in the presence of oleic acid.

### 3.2. Electrochemical properties of Co@CoO core-shell nanocrystals

The electrochemical properties of Co@CoO core-shell nanocrystals were analyzed by CV at room temperature. The electrochemical properties of the four kinds of Co@CoO core-shell nanocrystals catalysts with different morphologies were compared under the same condition (Fig. 5). The onset of the catalytic wave attributed to water oxidation is observed at 0.42 V (versus Ag/AgCl) for 1. However, the onset of the catalytic wave achieved was at approximately 0.36, 0.35 and 0.29 V for 2, 3 and 4. Moreover, we conducted a control experiment under the same condition, except without the presence of 1. By contrast, the CV result of the control experiment showed that only a minimum current was obtained in the same borate buffer solution. This evidence clearly demonstrated that 1 benefits for catalyzing the water oxidation reaction under irradiation.

### 3.3. Photocatalytic water oxidation by Co@CoO core-shell nanocrystals

Samples 1–4 of Co@CoO core-shell nanocrystals with different morphologies were shown to catalyze water oxidation to evolve O<sub>2</sub> by photoirradiation (Fig. 6). The O<sub>2</sub> rapidly evolved under visible light illumination, and the O<sub>2</sub> evolution amount achieved a maximum value within 6 min. Among the reactions of Co@CoO core-shell nanocrystals with different morphologies, maximum values of O<sub>2</sub> yield (96.6% for 1, 67.5% for 2, 90.0% for 3, and 21.9% for 4) and O<sub>2</sub> evolution amount (24.2 μmol for 1, 16.9 μmol for 2,

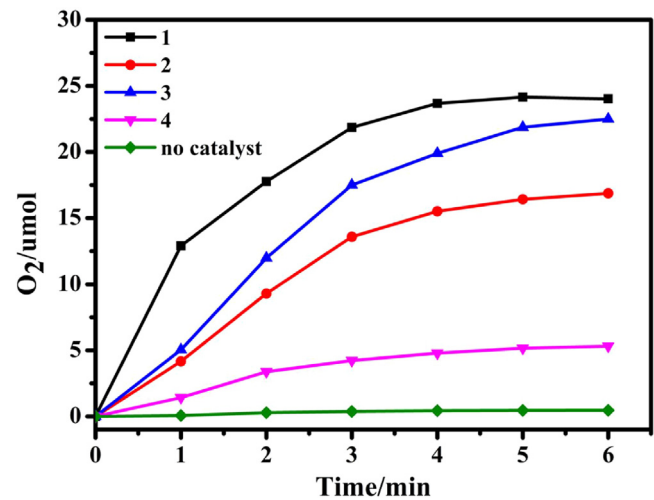


**Fig. 6.** Kinetics of O<sub>2</sub> evolution of the photocatalytic system using different morphologies of catalyst and without any catalyst: 1 (red); 2 (black); 3 (blue); 4 (pink); no catalyst (green). Conditions: 300 W Xe lamp equipped with a long-pass filter (420 nm cutoff); 1 mg catalysts, 1.0 mM [Ru(bpy)<sub>3</sub>]<sup>2+</sup>, 5.0 mM Na<sub>2</sub>S<sub>2</sub>O<sub>8</sub>, 80 mM sodium borate buffer (initial pH 9.0); total reaction volume 10 mL; vigorous stirring. (For interpretation of the references to color in this figure legend, the reader is referred to the web version of this article.)

**Table 1**  
Water oxidation catalyzed by catalysts 1–4 with different morphologies.

Catalysts	O <sub>2</sub> (μmol)	TOF[(mol <sub>O2</sub> mol <sub>metal</sub> <sup>-1</sup> s <sup>-1</sup> ) <sup>b</sup> ]
1 <sup>a</sup>	24.2	6.6 × 10 <sup>-3</sup>
2 <sup>a</sup>	16.9	2.1 × 10 <sup>-3</sup>
3 <sup>a</sup>	22.5	2.6 × 10 <sup>-3</sup>
4 <sup>a</sup>	5.3	7.2 × 10 <sup>-4</sup>

<sup>a</sup> Conditions: 300 W Xe lamp equipped with a long-pass filter (420 nm cutoff); catalysts (1 mg), [Ru(bpy)<sub>3</sub>]<sup>2+</sup> (1.0 mM), Na<sub>2</sub>S<sub>2</sub>O<sub>8</sub> (5.0 mM), borate buffer (80 mM, pH 9.0), total reaction solution volume: 10 mL; vigorous stirring.

<sup>b</sup> TOFs per metal ion were calculated for the first 60 s (TOF = mol of oxygen produced in 1 min mol<sup>-1</sup> of metal ion).

22.5 μmol for 3, and 5.3 μmol for 4) were achieved for 1 mg of 1–4 after 6 min illumination (Fig. 6 and Table 1). The initial rate of water oxidation corresponds to the described order of the catalytic activity of these catalysts. 1 was proven to be the best example of water oxidation catalyst. According to a series of characterization analysis, Co@CoO core-shell nanocrystals with different morphologies can significantly influence the catalytic performance, which arises from differences in polar planes or exposed active planes. Catalysts with higher surface energy show better catalytic performance [27,28]. The growth of crystals with some preferred structures or planes was controlled by the surface energy of the planes, and the planes with lower surface energy were liable to dominate over the others. The exposed active plane was also a crucial factor leading to the highest catalytic activity. 1 with spherical hierarchical structure showed the optimum catalytic activity among all the samples synthesized, presumably, resulting from the formation of nanocrystals with active plane and higher surface energy in this sample. The obtained Co@CoO core-shell nanocrystal 1 enclosed by high-energy {101} and {111} facets exhibited enhanced water oxidation catalytic activity, which may be attributed to that high-energy {101} and {111} facets having an open surface structure that provides more active sites (Fig. 3). In addition, the spherical hierarchical structure of Co@CoO 1 is conducive to catalysis: each sheet of Co@CoO core-shell nanoplates 1 is in nanoscale; thus, the catalytic surface of each sheet is effectively exposed out. In general, particles are easily aggregated when their sizes are very small, but the catalytic performance will be much less efficient when the particles

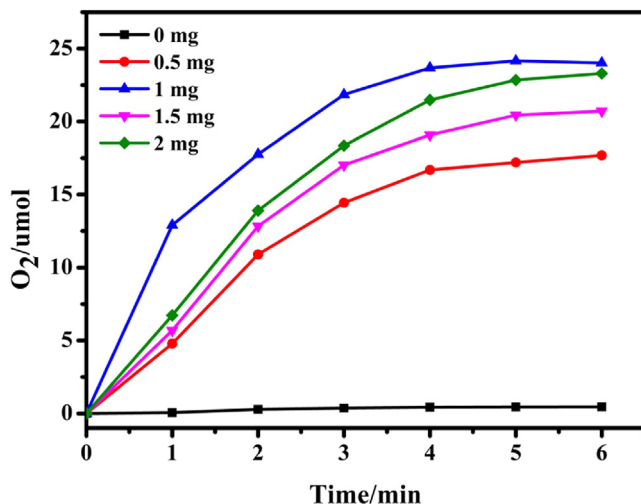


**Fig. 7.** Kinetics of  $O_2$  evolution of the photocatalytic system using different amount of Co@CoO core-shell nanocrystals 1 (0 mg (black); 0.5 mg (red); 1.0 mg (blue); 1.5 mg (pink); 2.0 mg (green)). Conditions: 300 W Xe lamp equipped with a long-pass filter (420 nm cutoff); 1.0 mM  $[Ru(bpy)_3](ClO_4)_2$ , 5.0 mM  $Na_2S_2O_8$ , 80 mM sodium borate buffer (initial pH 9.0); total reaction volume 10 mL; vigorous stirring. (For interpretation of the references to color in this figure legend, the reader is referred to the web version of this article.)

are very large. The spherical hierarchical structure is an effectively method to keep catalytic performance while prevent agglomeration. Furthermore, micron-sized spheres are demonstrated high catalytic efficiency in nanometer scale. Therefore, Co@CoO core-shell nanoplate 1 with spherical hierarchical structure presents highly catalytic activity.

The CV results also strongly support that 1 benefits for catalyzing the water oxidation reaction among the four Co@CoO core-shell nanocrystals catalysts with different morphologies (Fig. 5). The order of the electrocatalytic activities of the four catalysts corresponds to the described order of the  $O_2$  evolution amount of the investigated catalysts. The activity of 1 was also compared with other water oxidation catalysts under visible light irradiation (Table S2, ESI). The data clearly indicated 1 exhibited excellent activity for water oxidation among these catalysts. In addition, we observed a small amount of  $O_2$  evolution with the absence of any catalyst only after 6 min irradiation under the same experimental condition (Fig. 6 and Table S1, ESI). Furthermore, we conducted photocatalytic water oxidation reaction without light irradiation, and no  $O_2$  evolution detected even in the presence of 1 (Table S1, ESI).

#### 3.4. Catalytic behavior of Co@CoO core-shell nanocrystals 1 for photocatalytic water oxidation

To obtain the optimal conditions, we systematically investigated the variables of photocatalytic reaction, including pH, buffer types, and photosensitizers. We studied the effects of different amounts of 1 on the photocatalytic oxygen evolution as described in Fig. 7. To investigate the influence of pH on the  $O_2$  yield of the photocatalytic water oxidation with 1 as catalyst, the initial pH value of the borate buffer reaction solution was set ranging from 7.0 to 10.0 in the controlled experiments. The  $O_2$  evolution amount increased with pH values increasing up to 9.0 and decreased with higher pH value of 10.0 in the presence of Co@CoO core-shell nanocrystals catalyst 1 (Fig. 8). The  $O_2$  yield obtained under the condition of pH 10.0 (54.9%) was much lower than that obtained under the condition of pH 9.0 (96.6%). Typically, the high pH condition is thermodynamically favorable for water oxidation. However, this strategy is a competitive procedure in the reduction of  $[Ru(bpy)_3]^{3+}$  to  $[Ru(bpy)_3]^{2+}$ , leading to the degradation of the photosensitizer

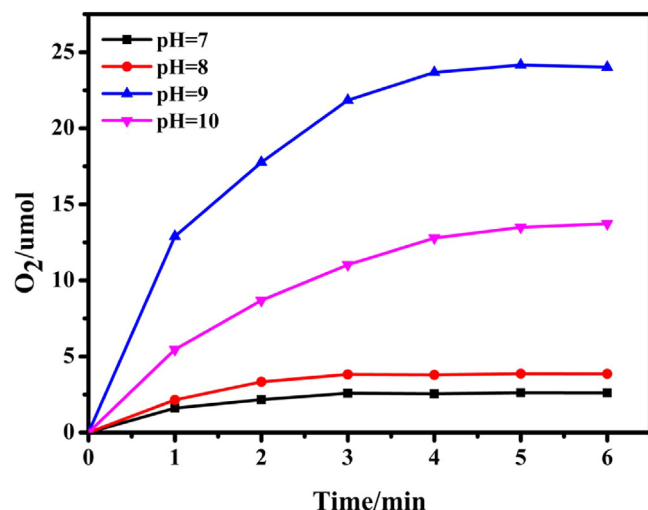
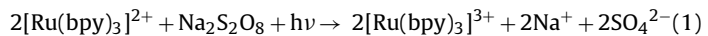
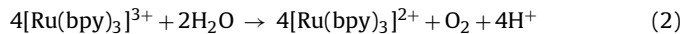


**Fig. 8.** Kinetics of  $O_2$  evolution of the photocatalytic system at different pHs of borate buffer (pH = 7 (black); pH = 8 (red); pH = 9 (blue); pH = 10 (pink)). Conditions: 300 W Xe lamp equipped with a long-pass filter (420 nm cutoff); 1 mg catalyst 1, 1.0 mM  $[Ru(bpy)_3](ClO_4)_2$ , 5.0 mM  $Na_2S_2O_8$ , 80 mM sodium borate buffer; total reaction volume 10 mL; vigorous stirring. (For interpretation of the references to color in this figure legend, the reader is referred to the web version of this article.)

[21,29,30]. The orange-red solution of  $[Ru(bpy)_3](ClO_4)_2$  turned green under light irradiation for 10 min, and this finding reflects the presence of  $[Ru(bpy)_3]^{3+}$  accumulation by visible light irradiation, as shown in Eq. (1):



We studied the existence of  $[Ru(bpy)_3]^{2+}$  and  $[Ru(bpy)_3]^{3+}$  by using UV-vis with their characteristic absorbance (Fig. 9 and Fig. S5, ESI). The results showed that the degradation of  $[Ru(bpy)_3]^{2+}$  and accumulation of  $[Ru(bpy)_3]^{3+}$ . In addition, the pH value of the solution was tested after the catalytic reaction, which decreased from 9.0 to 8.5 due to the generation of  $H^+$  in the catalytic process, as shown in Eq. (2):



Furthermore, we investigated the photocatalytic water oxidation activities of 1 mg catalysts in the presence of various photosensitizers and buffers (Figs. S3 and S4, ESI). These results demonstrated that the reaction environment can significantly influence the photocatalytic water oxidation activities of the catalysts.

#### 3.5. Decomposition of the photosensitizer

The photosensitizer can be self-quenched and decomposed by a nucleophilic attack of  $OH^-$  or water on  $Ru(bpy)_3^{3+}$  under neutral or basic conditions. This phenomenon is a competition process to hole transfer from  $Ru(bpy)_3^{3+}$  to water oxidation catalysts. Moreover, this process is a key step leading to the decomposition of the photosensitizer and limiting the oxygen evolution [30]. Therefore, a better efficient water oxidation catalyst should be developed to improve the lifetime of the photosensitizer and  $O_2$  evolution yield consequently [21,31,32].  $Ru(bpy)_3^{2+}$  was demonstrated to be exist from the accordance with its characteristic absorbance by UV-vis (Fig. 9). After 10 min illumination, the concentration of  $Ru(bpy)_3^{2+}$  photosensitizer was markedly decomposed (30% of the initial concentration) in the absence of the catalyst. By contrast, the concentration decreased by 6.7% in the presence of catalyst 1 after illumination for 10 min under the same condition. The UV-vis evi-

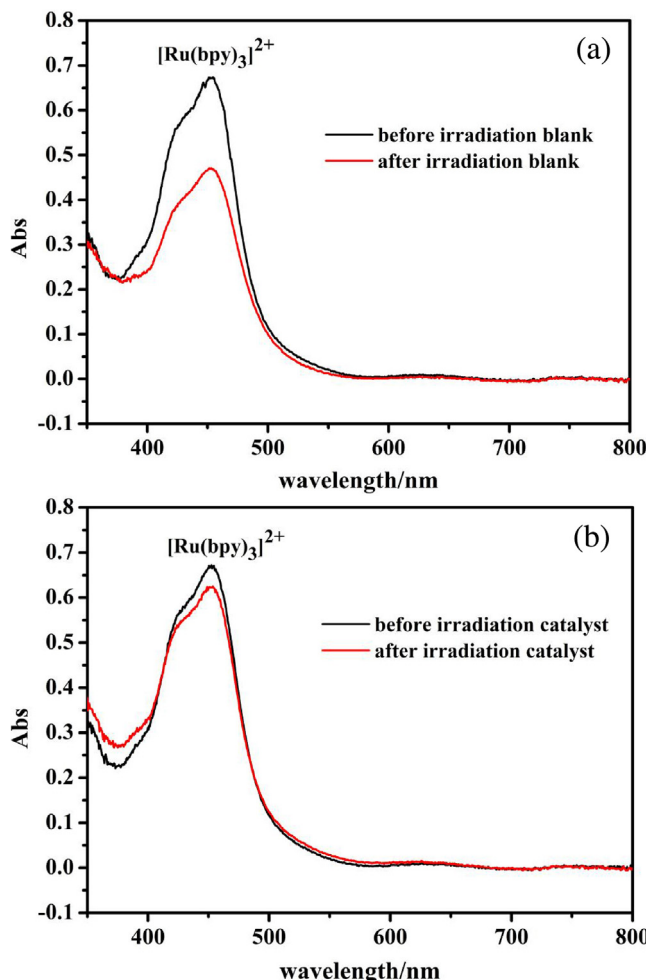


**Fig. 9.** (a) UV-vis spectral changes during the photocatalytic  $\text{O}_2$  evolution without any catalyst. The black line shows the absorption of aqueous borate buffer solutions ( $\text{pH} = 9.0$ ,  $4.0 \text{ mM}$ ) containing  $[\text{Ru}(\text{bpy})_3](\text{ClO}_4)_2$  ( $50 \mu\text{M}$ ) and  $\text{Na}_2\text{S}_2\text{O}_8$  ( $250 \mu\text{M}$ ). The red line shows the absorption of above solution after  $10 \text{ min}$  of irradiation. (b) UV-vis spectral changes during the photocatalytic  $\text{O}_2$  evolution with 1. The black line shows the absorption of aqueous borate buffer solutions ( $\text{pH} = 9.0$ ,  $4.0 \text{ mM}$ ) containing  $[\text{Ru}(\text{bpy})_3](\text{ClO}_4)_2$  ( $50 \mu\text{M}$ ),  $\text{Na}_2\text{S}_2\text{O}_8$  ( $250 \mu\text{M}$ ) and catalyst 1 ( $0.05 \text{ mg}$ ). The red line shows the absorption of above solution after  $10 \text{ min}$  of irradiation. (For interpretation of the references to color in this figure legend, the reader is referred to the web version of this article.)

dence strongly indicated that the photosensitizer  $[\text{Ru}(\text{bpy})_3]^{2+}$  can be efficiently protected from decomposition in the presence of 1.

### 3.6. Reuse of $\text{Co}@\text{CoO}$ core-shell nanoplates 1

1 was reused under the optimal conditions after the first completion of the catalytic experiment. The catalysts can be easily separated and recovered by a magnet on account of its ferromagnetic properties (Fig. S6, ESI). In the second run, the recovered catalysts remained active with the nearly same  $\text{O}_2$  evolution amount (Fig. 10). Even after the sixth run, the high catalytic activity of the recovered 1 remained. This  $\text{O}_2$  evolution amount of the sixth run using the recovered catalysts was 21.8, which maintained 90% of the fresh catalysts. This lower  $\text{O}_2$  evolution amount may be ascribed to the loss of catalytic particles during the recovery process [33,34].

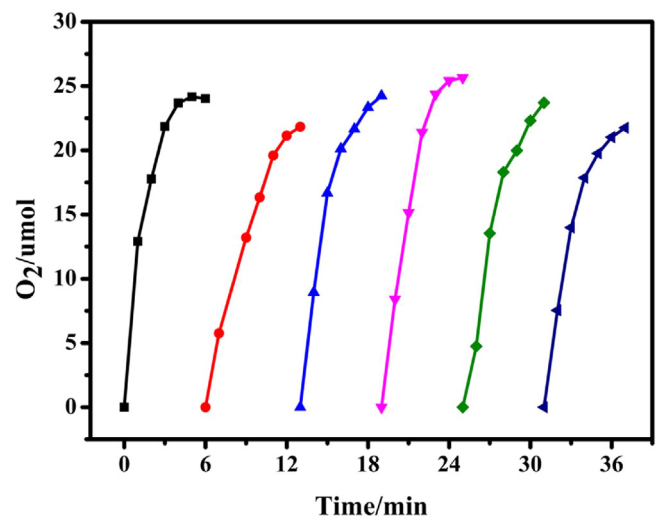


**Fig. 10.** Kinetics of  $\text{O}_2$  formation in the photocatalytic system using fresh 1 and recovered 1. First run (black); second run (red); third run (blue); fourth run (pink); fifth run (green); sixth run (purple). Conditions:  $300 \text{ W}$  Xe lamp equipped with a long-pass filter (420 nm cutoff);  $1 \text{ mg}$  catalyst,  $1.0 \text{ mM}$   $[\text{Ru}(\text{bpy})_3](\text{ClO}_4)_2$ ,  $5.0 \text{ mM}$   $\text{Na}_2\text{S}_2\text{O}_8$ ,  $80 \text{ mM}$  sodium borate buffer (initial  $\text{pH} 9$ ); total reaction volume is  $10 \text{ mL}$ ; vigorous agitation using a magnetic stirrer. (For interpretation of the references to color in this figure legend, the reader is referred to the web version of this article.)

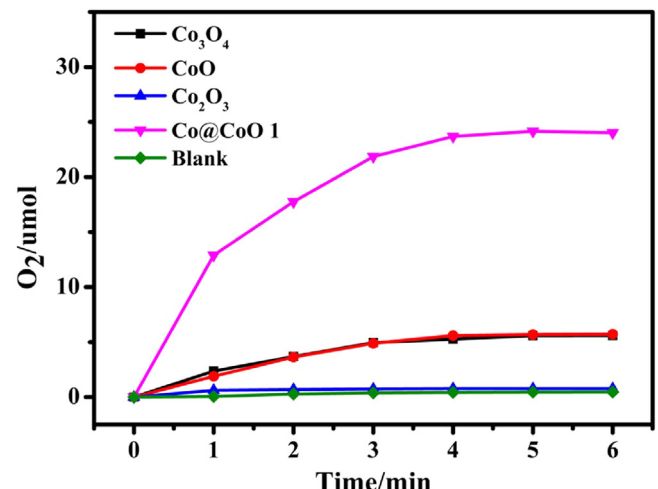


**Fig. 11.** Kinetics of  $\text{O}_2$  evolution of the photocatalytic system using different catalysts:  $\text{Co}_3\text{O}_4$  (black);  $\text{CoO}$  (red);  $\text{Co}_2\text{O}_3$  (blue);  $\text{Co}@\text{CoO}$  1 (pink); Blank (green). Conditions:  $300 \text{ W}$  Xe lamp equipped with a long-pass filter (420 nm cutoff);  $1 \text{ mg}$  catalysts,  $1.0 \text{ mM}$   $[\text{Ru}(\text{bpy})_3](\text{ClO}_4)_2$ ,  $5.0 \text{ mM}$   $\text{Na}_2\text{S}_2\text{O}_8$ ,  $80 \text{ mM}$  sodium borate buffer (initial  $\text{pH} 9.0$ ); total reaction volume  $10 \text{ mL}$ ; vigorous stirring. (For interpretation of the references to color in this figure legend, the reader is referred to the web version of this article.)

### 3.7. Photocatalytic water oxidation with different cobalt oxides

The kinetics of  $\text{O}_2$  evolution of the photocatalytic system with different cobalt oxides were shown in Fig. 11. The  $\text{O}_2$  evolution amount of obtained after the reaction with  $\text{Co}@\text{CoO}$  core-shell nanocrystals catalyst 1 ( $24.2 \text{ mmol}$ ) was larger than that with  $\text{CoO}$  ( $5.7 \mu\text{mol}$ ),  $\text{Co}_2\text{O}_3$  ( $0.8 \mu\text{mol}$ ) and  $\text{Co}_3\text{O}_4$  ( $5.6 \mu\text{mol}$ ). The TOF of  $\text{Co}@\text{CoO}$  core-shell nanocrystal catalyst 1 was  $6.6 \times 10^{-3} \text{ mol}_{\text{O}_2} \text{ mol}_{\text{metal}}^{-1} \text{ s}^{-1}$ , which was significantly higher than that with  $\text{CoO}$  ( $2.4 \times 10^{-3}$ ),  $\text{Co}_2\text{O}_3$  ( $8.6 \times 10^{-4}$ ) and  $\text{Co}_3\text{O}_4$  ( $3.5 \times 10^{-3}$ ) (Table S3, ESI). These results clearly demonstrated that 1 exhibited much higher activity than other cobalt oxides catalysts.

To further study the interface electron transfer rate of the different catalysts, the electrochemical impedance spectroscopy (EIS) was conducted (Fig. S7). The EIS experiment was carried out by applying an AC voltage with 10 mV amplitude in a frequency ranging from 100000 to 0.1 Hz in the borate buffer solution (80 mM, pH = 9.0). It was found that the arc diameter of catalyst 1 was much smaller than other catalysts. This smaller arc radius on the EIS Nyquist plot of catalyst 1 indicated that separation of photogenerated electron-hole pairs of 1 is more effective and interfacial charge transfer of 1 is faster than other cobalt oxides. The result of EIS demonstrated that 1 has higher electrocatalytic water oxidation activity than that of CoO, Co<sub>3</sub>O<sub>4</sub> and Co<sub>2</sub>O<sub>3</sub>. The result of the EIS experiment of the four catalysts is consistent with the described order of the O<sub>2</sub> evolution amount for the photocatalytic water oxidation using the four samples.

### 3.8. Stability studies on Co@CoO core-shell nanocrystals 1

Recently, the stability of water oxidation catalysts in the reaction has become a very critical issue for researchers. Through the interfacial reaction of Co(acac)<sub>3</sub> with hydrazine hydrate under hydrothermal conditions, many small metal clusters (nuclei) form simultaneously for the short lifetime of monomers in the solution. By dynamically coating the particles with a close-packed monolayer of coordinating ligand, the surfactant can control the size and shape of the growing crystals; the surface tension decreased, and the growth can be modified through charge transfer.

1 was characterized before and after the reaction by PXRD (Fig. S8, ESI) measurements. PXRD patterns of catalyst 1 after the oxygen evolution reaction did not show any change compared with the fresh catalyst. These analysis results indicated that catalyst 1 is highly efficient and stable during the photocatalytic reaction.

XPS measurements were performed to investigate the change in the surface conditions of catalyst 1 before and after the photocatalytic reaction (Fig. 12). The XPS spectra of C 1s, O 1s, and Co 2p core levels and full scan were obtained. The Co 2p XPS spectra are shown in Fig. 12a, the peaks at 779.1 and 794.0 eV are observed after the reaction. Two peaks at 781.6 and 796.7 eV with two satellite peaks at 786.4 and 803.6 eV are also shown in the XPS spectra of Co 2p in Fig. 12a. The XPS shows similar regions of the peak between the Co 2p main peak and the satellite peak for both samples before and after the reaction. The same binding energy ascribed to Co<sup>2+</sup> before and after the reaction strongly demonstrate that there is no change in the valence state of Co<sup>2+</sup>. No changes in the surface conditions of Co@CoO 1 before and after the reaction are also confirmed by the absence of a shift in the O 1s peak (Fig. 12c). Therefore, Co@CoO 1 is highly robust catalyst in the photocatalytic water oxidation.

We investigated the kinetics of oxygen evolution contrast tests (Fig. S9, ESI). The catalysts aged for 3 h evolved 24.1 μmol O<sub>2</sub>, which is almost the same as that of the fresh catalysts (24.2 μmol O<sub>2</sub>). This finding indicated that 1 is stable in buffer solution.

Further evidence of active species was given by measuring the remaining cobalt ion concentration in the supernatant post-catalytic reaction solution with Atomic Absorption Spectrometry (AAS). The AAS result showed a very small amount of Co ion exudation of 0.11% from 1. To rule out the effects of dissociated Co ions on the catalytic activities of 1 in the photocatalytic water oxidation reaction, we conducted the catalytic reaction with an isolated supernatant. A very small amount of O<sub>2</sub> evolved in the presence of the supernatant (Fig. S11, ESI). This result demonstrated that minimum exudation Co ions only produced a very small amount of O<sub>2</sub> and cannot affect the photocatalytic activity of 1.

Dynamic light scattering (DLS) measurements were conducted to test the reaction solution before and after irradiation of 60 min with a 300 W Xe lamp equipped with a long-pass filter (420 nm cutoff). The analysis data of the DLS measurement indicated that

no nanoparticles were found ranging from several nanometers to a thousand nanometers after photocatalytic water oxidation (Fig. S12, ESI). Therefore, the results confirmed that Co@CoO core-shell nanocrystal 1 is stable during the photocatalytic water oxidation process.

The catalytic activity of cobalt oleate for the photocatalytic water oxidation was further examined. However, the amount of O<sub>2</sub> evolution was approximately 9.1 μmol, which was only 37.6% of that with 1 (Fig. S13, ESI). The results clearly revealed that cobalt oleate did not act as an efficient catalyst as that of 1.

The following experiments were conducted to elucidate the nature of the catalytic species in light-driven water oxidation by 1. The supernatant after the light-driven water oxidation reaction was recovered by centrifugation and then measured by liquid chromatography-mass spectrometry (Fig. S14, ESI). The species analyzed in the mass spectrum were ClO<sub>4</sub><sup>−</sup>: *m/z* = 99.5 and [Ru(py)<sub>3</sub>](ClO<sub>4</sub>)<sub>2</sub>: *m/z* = 534 (py = pyridine). No other cobalt species were found by the mass spectrum analysis data. The measurement results provide strong evidence that 1 demonstrates oxidative and hydrolytic stability for the photocatalytic water oxidation process.

### 3.9. Mechanistic study

The mechanism of the light-driven water oxidation is illustrated in Scheme 1. Photosensitizer [Ru(bpy)<sub>3</sub>]<sup>2+</sup> absorbs photons and converts them into excited state [Ru(bpy)<sub>3</sub>]<sup>2\*+</sup> (where \* denotes the excited state) under visible light illumination. Subsequently, [Ru(bpy)<sub>3</sub>]<sup>2\*+</sup> were quenched by Na<sub>2</sub>S<sub>2</sub>O<sub>8</sub> through electrons transferred from [Ru(bpy)<sub>3</sub>]<sup>2\*+</sup> to S<sub>2</sub>O<sub>8</sub><sup>2−</sup>, resulting in the generation of SO<sub>4</sub><sup>2−</sup>, [Ru<sup>III</sup>(bpy)<sub>3</sub>]<sup>3+</sup> complexes and SO<sub>4</sub><sup>•−</sup> radical anions. The SO<sub>4</sub><sup>•−</sup> radical anions {[E<sup>0</sup>(SO<sub>4</sub><sup>•−</sup>/SO<sub>4</sub><sup>2−</sup>) = +2.40 V vs. Ag/AgCl]} also act as strong oxidants [35]. The electrode potential of the SO<sub>4</sub><sup>•−</sup> radical anions is higher than that of {[E<sup>0</sup>([Ru(bpy)<sub>3</sub>]<sup>2+</sup>/[Ru(bpy)<sub>3</sub>]<sup>3+</sup>) = +1.12 V vs. Ag/AgCl]} [36,37], leading the oxidation of other [Ru(bpy)<sub>3</sub>]<sup>2+</sup> to more amount of [Ru<sup>III</sup>(bpy)<sub>3</sub>]<sup>3+</sup>. Finally, electrons are captured by [Ru(bpy)<sub>3</sub>]<sup>3+</sup> from catalysts; water was oxidized to the evolving O<sub>2</sub>.

## 4. Conclusions

In summary, a simple and easy method was developed to fabricate magnetic Co@CoO core-shell nanocrystals with the desired structure via a one-pot toluene-water two-phase interfacial reaction. An efficient photocatalytic water oxidation reaction system was presented using [Ru(bpy)<sub>3</sub>]<sup>2+</sup> as a photosensitizer, Na<sub>2</sub>S<sub>2</sub>O<sub>8</sub> as a sacrificial electron acceptor, and borate as a buffer solution at pH 9.0 in the presence of Co@CoO core-shell nanocrystals under visible light irradiation. The catalytic behaviors of 1–4 with different morphologies were compared in terms of photocatalytic water oxidation. Co@CoO 1 with a spherical hierarchical structure was observed as a highly efficient water oxidation catalyst with a high O<sub>2</sub> yield over 96% under optimal conditions. The spherical hierarchical structure is beneficial to catalysis because of the complete use of the catalytic surface of each nanoscale sheet. Moreover, agglomeration is prevented and high catalytic efficiency in nanometers for micron-sized spheres is promoted. CV results also strongly demonstrated that 1 exhibits the best activity for catalyzing the water oxidation reaction among the four Co@CoO core-shell nanocrystals catalysts with different morphologies. The order of the electrocatalytic activities of the four catalysts corresponds to the described O<sub>2</sub> evolution amount of the photocatalytic water oxidation over these catalysts. Present research provides a simple basis for Co@CoO core-shell nanocrystals preparation to obtain excellent water oxidation catalysts. This study also presents a reference for

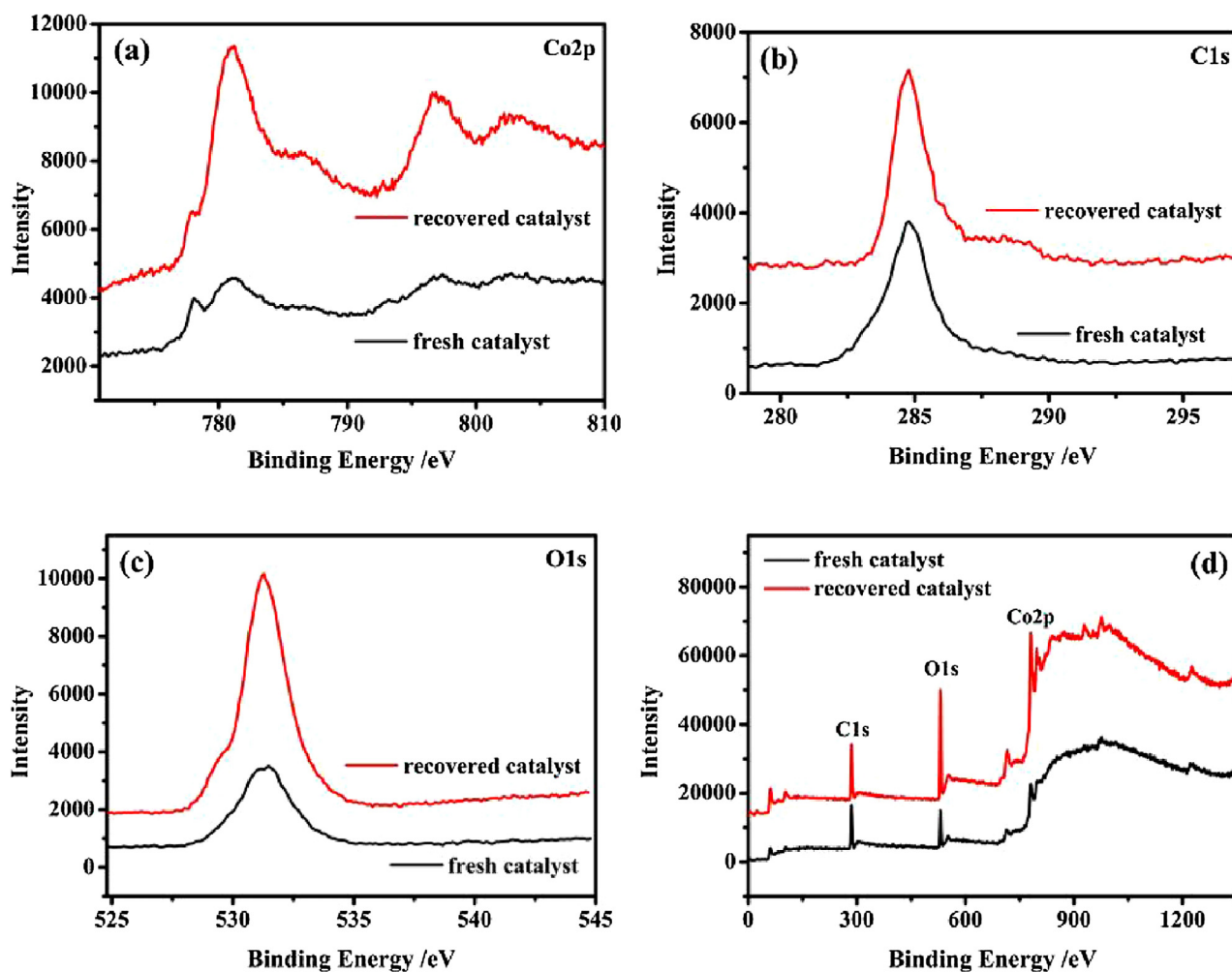
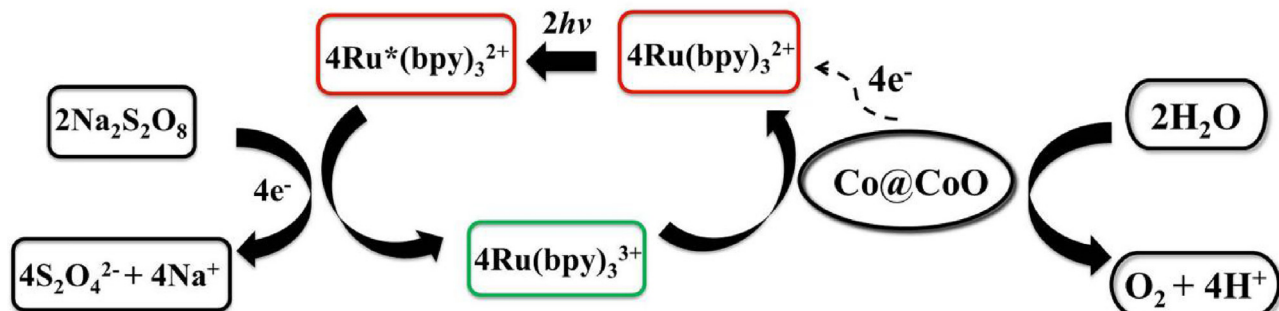


**Fig. 12.** X-ray photoelectron spectra of catalyst 1 before and after the reaction in the energy regions of Co 2p (a), C1s (b), O 1s (c) and full scan (d) of catalyst 1 before and after the reaction.



**Scheme 1.** The processes of photocatalytic water oxidation catalyzed by  $\text{Co}@\text{CoO}$  core-shell nanocrystals.

the design, synthesis, and upgrade of other structurally enhanced catalysts.

### Acknowledgements

We acknowledge funding support from National Natural Science Foundation of China (No. 21162027, 21261022 and 21173105) and The Hunan Provincial Science and Technology Plan Project, China (No. 2016TP1007).

### Appendix A. Supplementary data

Supplementary data associated with this article can be found, in the online version, at <http://dx.doi.org/10.1016/j.apcatb.2017.03.056>.

### References

- [1] G.D. Scholes, G.R. Fleming, A. Olaya-Castro, R. van Grondelle, *Nat. Chem.* 3 (2011) 763–774.
- [2] M.D. Symes, L. Cronin, *Nat. Chem.* 5 (2013) 403–409.

- [3] X. Chen, C. Li, M. Grätzel, R. Kostecki, S.S. Mao, *Chem. Soc. Rev.* 41 (2012) 7909–7937.
- [4] C. Wang, K.E. deKrafft, W. Lin, *J. Am. Chem. Soc.* 134 (2012) 7211–7214.
- [5] Y. Umena, K. Kawakami, J.-R. Shen, N. Kamiya, *Nature* 473 (2011) 55–60.
- [6] M.W. Kanan, D.G. Nocera, *Science* 321 (2008) 1072–1075.
- [7] F.M. Toma, A. Sartorel, M. Iurlo, M. Carraro, P. Parisse, C. Maccato, S. Rapino, B.R. Gonzalez, H. Amenitsch, T. Da Ros, *Nat. Chem.* 2 (2010) 826–831.
- [8] R. Brimblecombe, G.F. Swiegers, G.C. Dismukes, L. Spiccia, *Angew. Chem. Int. Ed.* 47 (2008) 7335–7338.
- [9] J.J. Concepcion, J.W. Jurss, M.K. Brennaman, P.G. Hoertz, A.O.T. Patrocinio, N.Y. Murakami Iha, J.L. Templeton, T.J. Meyer, *Acc. Chem. Res.* 42 (2009) 1954–1965.
- [10] D. Shevchenko, M.F. Anderlund, A. Thapper, S. Styring, *Energy Environ. Sci.* 4 (2011) 1284–1287.
- [11] T. Nakagawa, N.S. Bjorge, R.W. Murray, *J. Am. Chem. Soc.* 131 (2009) 15578–15579.
- [12] W.C. Ellis, N.D. McDaniel, S. Bernhard, T.J. Collins, *J. Am. Chem. Soc.* 132 (2010) 10990–10991.
- [13] J.L. Fillol, Z. Codolà, I. Garcia-Bosch, L. Gómez, J.J. Pla, M. Costas, *Nat. Chem.* 3 (2011) 807–813.
- [14] L. Chi, Q. Xu, X. Liang, J. Wang, X. Su, *Small* 12 (2016) 1351–1358.
- [15] F. Song, Y. Ding, B. Ma, C. Wang, Q. Wang, X. Du, S. Fu, J. Song, *Energy Environ. Sci.* 6 (2013) 1170.
- [16] F. Jiao, H. Frei, *Angew. Chem. Int. Ed.* 48 (2009) 1841–1844.
- [17] M. Zhang, Y.-L. Huang, J.-W. Wang, T.-B. Lu, *J. Mater. Chem. A* 4 (2016) 1819–1827.
- [18] Q. Xu, H. Li, F. Yue, L. Chi, J. Wang, *New J. Chem.* 40 (2016) 3032–3035.
- [19] Q. Xu, H. Li, L. Chi, L. Zhang, Z. Wan, Y. Ding, J. Wang, *Appl. Catal. B: Environ.* 202 (2017) 397–403.
- [20] J. Wei, Y. Feng, Y. Liu, Y. Ding, *J. Mater. Chem. A* 3 (2015) 22300–22310.
- [21] D. Hong, J. Jung, J. Park, Y. Yamada, T. Suenobu, Y.-M. Lee, W. Nam, S. Fukuzumi, *Energy Environ. Sci.* 5 (2012) 7606–7616.
- [22] D. Hong, S. Mandal, Y. Yamada, Y.-M. Lee, W. Nam, A. Llobet, S. Fukuzumi, *Inorg. Chem.* 52 (2013) 9522–9531.
- [23] C. Li, K. Shuford, Q. Park, W. Cai, Y. Li, E. Lee, S. Cho, *Angew. Chem.* 46 (2007) 3264 (International ed. in English).
- [24] W. Niu, S. Zheng, D. Wang, X. Liu, H. Li, S. Han, J. Chen, Z. Tang, G. Xu, *J. Am. Chem. Soc.* 131 (2009) 697–703.
- [25] W. Niu, L. Zhang, G. Xu, *Acs Nano* 4 (2010) 1987–1996.
- [26] Y.J. Zhang, Q. Yao, Y. Zhang, T.Y. Cui, D. Li, W. Liu, Z.D. Zhang, *Cryst. Growth Des.* 8 (2008) 3206–3212.
- [27] J. Zhang, K. Sasaki, E. Sutter, R. Adzic, *Science* 315 (2007) 220–222.
- [28] G. Li, T. Hu, G. Pan, T. Yan, X. Gao, H. Zhu, *J. Phys. Chem. C* 112 (2008) 11859–11864.
- [29] P.K. Ghosh, B.S. Brunschwig, M. Chou, C. Creutz, N. Sutin, *J. Am. Chem. Soc.* 106 (1984) 4772–4783.
- [30] C. Creutz, N. Sutin, *Proc. Natl. Acad. Sci.* 72 (1975) 2858–2862.
- [31] N.D. Morris, T.E. Mallouk, *J. Am. Chem. Soc.* 124 (2002) 11114–11121.
- [32] D. Hong, Y. Yamada, A. Nomura, S. Fukuzumi, *Phys. Chem. Chem. Phys.* 15 (2013) 19125–19128.
- [33] D. Ressig, M. Shalom, J. Patscheider, R. Moré, F. Evangelisti, M. Antonietti, G.R. Patzke, *J. Mater. Chem. A* 3 (2015) 5072–5082.
- [34] M. Grzelczak, J. Zhang, J. Pfrommer, J. Hartmann, M. Driess, M. Antonietti, X. Wang, *ACS Catal.* 3 (2013) 383–388.
- [35] Y. Yamada, K. Yano, D. Hong, S. Fukuzumi, *Phys. Chem. Chem. Phys.* 14 (2012) 5753–5760.
- [36] C. Creutz, N. Sutin, *Inorg. Chem.* 15 (1976) 496–499.
- [37] H. Lv, J. Song, H. Zhu, Y.V. Geletii, J. Bacs, C. Zhao, T. Lian, D.G. Musaev, C.L. Hill, *J. Catal.* 307 (2013) 48–54.